IEEE Access
Multidisciplinary | Rapid Review | Open Access Journal

Received May 15, 2017, accepted May 29, 2017, date of publication June 20, 2017, date of current version July 3, 2017.

Digital Object Identifier 10.1109/ACCESS.2017.2715011

Locally Linear Embedding-Based Motion Estimation From Truncated Projections for Computed Tomography

MIAOSHI WANG[1,2], SHUXU GUO[1], AND HENGYONG YU[2], (Senior Member, IEEE)
[1]College of Electronic Science and Engineering, Jilin University, Changchun 130012, China
[2]Department of Electrical and Computer Engineering, University of Massachusetts Lowell, Lowell, MA 01854 USA

Corresponding author: Hengyong Yu (hengyong-yu@ieee.org)

This work was supported by the NSF CAREER Award CBET-1540898.

ABSTRACT In the computed tomography (CT) field, image reconstructions from truncated projections acquired by only illuminating the region of interest are an effective method to reduce the radiation dose. Theoretically, it has been proven that the exact interior reconstruction is feasible with some prior knowledge. However, the traditional data-consistency-based motion correction methods cannot be applied to truncated data. In this paper, we propose a locally linear embedding (LLE)-based motion correction method for locally truncated projections. Compared with the fast rotation of the X-ray source, the object motion is relatively slow and can be approximated by a smooth polynomial function. Based on this knowledge, a constraint term is added to optimize the estimated motion parameters. Extensive numerical simulations are performed. Our results demonstrate the feasibility and satisfactory performance of the proposed method. As far as the authors know, this algorithm is the first of its kind for motion parameter estimation only from truncated projections in the CT field.

INDEX TERMS Truncated projection, motion correction, locally linear embedding.

I. INTRODUCTION

Computed tomography (CT) has been widely accepted to detect the interior structures of objects. Particularly in clinical applications, CT images provide important information to help physicians make correct diagnostic decisions. However, X-rays are harmful and may induce genetic, cancerous and other diseases, which limits the extension of CT for clinical applications. To maximize the benefits of CT, the as-low-as-reasonably achievable principle is widely accepted in clinics, and several solutions have been proposed for dose reduction. For example, we can only illuminate a region-of-interest (ROI) and reconstruct images from truncated projections.

Theoretically, exact reconstruction can be performed from truncated projections under some conditions. The well-known two-step Hilbert transform method developed by Noo *et al.* [1] in 2004 is considered a milestone work for image reconstruction from truncated projections. Based on their algorithm, an image in the field of view (FOV) can be exactly reconstructed along a PI segment if two endpoints of the PI-segment are outside the convex hull of the image object support. Then, Defrise *et al.* relaxed this condition in 2006. They concluded that an exact reconstruction was available if one endpoint of the PI segment was outside the object support [2]. Later, Ye *et al.* proved that if a sub-region in the FOV was known, the interior problem for ROI could be exactly and stably solved. The aforementioned algorithms assume some special prior knowledge, which may lead to certain limitation in practical applications. In 2009, more general results were reported. Inspired by the compressive sensing (CS) theory, it was proven that the exact solution for an interior problem can be determined if the ROI is piecewise constant or piecewise polynomial [3]–[7]. Because most human organs can be approximated as piecewise constant regions, the CS-based algorithms have wide applications.

Motion is sometimes inevitable in practice during a CT scan. For example, infant and seriously injured patients cannot remain stationary during the entire scanning procedure. Many studies have been performed to reduce the motion artifacts. For example, we can improve temporal resolution by increasing the source rotation speed or using multiple X-ray sources [8], [9]. Minimizing the contribution of the views with obvious motion is also a popular method [10], [11]. However, these methods cannot thoroughly eliminate the

motion artifacts. Therefore, it is necessary to develop algorithms to compensate for motion artifacts by estimating the motion parameters. The available algorithms can be divided into two categories: analytical methods [12]–[14] and iterative methods [15]. In general, analytical methods are based on the data consistency condition (DCC) because of the redundancy of CT projections. The Helgason-Ludwig consistency condition (HLCC), which is the well-known DCC in the CT field for two-dimensional (2D) parallel beam projection data, can be applied for motion artifact reduction. During recent decades, many other DCCs were proposed [16]–[18] for different projection geometries. Furthermore, several iterative algorithms were developed. In 2008, Panetta *et al.* [19] proposed an optimization-based geometrical calibration algorithm, which is appropriate for cone-beam projection. In 2009, Patel *et al.* [20] proposed a motion correction method for a cone-beam micro-CT system, which also only demands the raw projection data. In 2016, Chen *et al.* [21] proposed a locally linear embedding (LLE)-based geometrical calibration method for fan-beam geometry. Using the derivative of re-projection with respect to the motion parameter, Sun *et al.* [22] developed another motion correction algorithm for helical geometry in 2016. Although the existing analytical and iterative methods work well, they assume that the projections are nontruncated. For the interior problem, they fail, or their performances are significantly compromised.

On one hand, many methods are available to solve the interior problem to reconstruct an ROI from truncated projections. On the other hand, as far as the authors know, there is no practical algorithm to estimate the motion parameters for motion artifact reductions from locally truncated projections. To conquer this difficulty, a new algorithm is required. In 2014, Clackdoyle and Desbat [23] constructed a new integral-type DCC assuming a parallel-beam geometry, which can be applied to truncated projections. Yu *et al.* [24] improved Clackdoyle and Desbat's result by extending it to a generalized condition that is suitable for 2D fan-beam geometry and general scanning trajectory. This generalized DCC by Yu *et al.* provides a method for geometrical calibration and motion estimation from a set of locally truncated projections. However, it is only valid when the origin is outside the convex support of the imaging objects. Because the origin is located inside imaging objects for most practical problems, it is of high significance to develop an algorithm to estimate the motion parameters from locally truncated projections. This issue motivated us to develop the LLE-based method described in this paper.

According to the LLE theory, because of the redundancy of projection, one can map a high-dimensional projection space into a low-dimensional motion-parameter space. Here, the key is how to address the data truncation in the framework of LLE for dimensionality reduction. In fact, the truncated projections are also redundant and can be processed by dimensional reduction. However, we find that the truncated projections can cause obvious deviations on the corrected motion parameters. Therefore, a polynomial-based regularization is introduced to make the motion trajectory converge to a smooth curve. This regularization is the key contribution of our paper. The remainder of this paper is organized as follows. In Section II, we describe the LLE-based algorithm in detail for motion estimation. In Section III, we demonstrate the feasibility of the proposed algorithm for truncated projections with numerical simulations. In Section IV, we discuss some related issues and conclude the paper.

II. METHOD

In general, an image has dimensions of $W \times H$, which represent the width and height of the image, respectively. The acquired sinogram dimension is $W_D \times V$, which represent the width of the detector and the amount of projections. A 2D CT reconstruction problem can be modeled as a linear system

$$Au = b, \tag{1}$$

where u is an image, b is the corresponding sinogram, and A is the system matrix. Both u and b in Eq. (1) are stretched into vectors, whose dimensions are $N = W \times H$ and $M = W_D \times V$. Although u and b are vectors, we prefer to call them the image and sinogram to avoid confusion. The relationship between u and b is determined by the system matrix A, which contains $M \times N$ elements. For any element $a_{m,n}$, its value represents the contribution of the n^{th} image pixel to the m^{th} projection value. The system matrix is determined by geometric parameters and motion parameters, which include translation t and rotation θ. t is a matrix consisting of two vectors that represent the translations along the x and y directions, and θ is a vector. These three vectors have identical lengths of V. The v^{th} element in any of the aforementioned vectors corresponds to the v^{th} projection view b_v. b_v is a vector with length W_D, and all b_v ($v = 1, 2, \cdots, V$) form projection vector b in Eq. (1). The geometric parameters of a given CT system are fixed. Thus, the value of system matrix A is a function of variables t and θ,

$$A = A(t, \theta). \tag{2}$$

Because the behaviors of A, u and re-projection $\tilde{b}$ are consistent, u and $\tilde{b}$ can also be treated as functions of motion parameters t and θ. With these known conditions, we can establish a motion parameter estimation algorithm for truncated projections as follows

$$(t, \theta) = \arg\min_{t,\theta} \left\| b - \tilde{b}(t, \theta) \right\|_2^2, \quad s.t.\ A(t, \theta)u(t, \theta) = b. \tag{3}$$

To solve Eq. (3), we propose a two-step method that consists of image update and motion parameter update. They are alternatively implemented as follows.

A. IMAGE UPDATE

In this section, image reconstruction is slightly different from the conventional method. A reconstructed image commonly represents a stable object. However, in our study, the

imaging object continuously moves, and different projection views correspond to different object positions. If we perform back-projection as usual, many interpolation operations are required to compensate the translation and rotation for one discrete image, and the interpolation operations can cause deviations, which decrease the image reconstruction performance. To solve this problem, we fix the object and move the system coordinate.

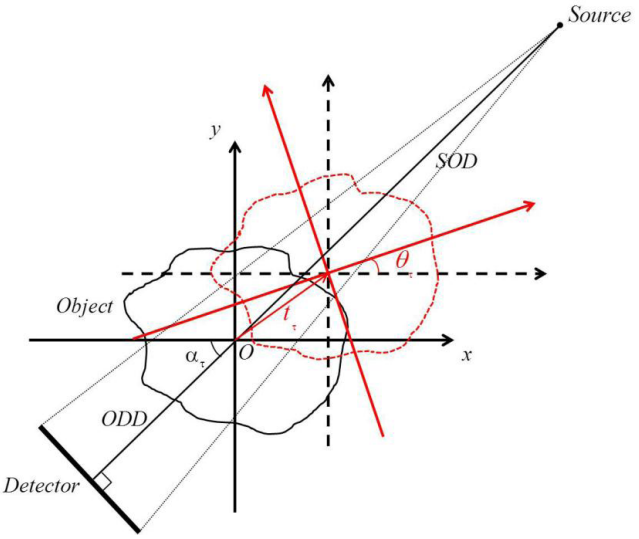

FIGURE 1. Sketch map for the object motion at time τ. The solid line represents the original object pose and the dashed line corresponds to the object pose at moment τ.

Figure 1 shows an example at moment τ: the X-ray source rotates an angle α_τ, the object translates t_τ and rotates θ_τ. Because of the principle of relative motion, we treat the object coordinate as the global coordinate. To represent the coordinates of the detector and source in conformity with the global coordinate, they must be translated along the opposite direction of t_τ and subsequently clockwise rotated in θ_τ around the global origin. This transformation of coordinates can be analytically accomplished with no approximation. As a result, we can accurately reconstruct the image at time 0.

The ordered-subset simultaneous algebraic reconstruction technique (OS-SART) [25] is used to reconstruct a CT image within the ordered subsets. The so-called ordered subset is to partition the index set $B = \{1, 2, \ldots, M\}$ into T nonempty disjoint subsets $B_s = \{\mathrm{m}_1^s, \mathrm{m}_2^s, \ldots, \mathrm{m}_{M(s)}^s\}$ such that

$$B = \bigcup_{0 \le s \le T-1} B_s. \tag{4}$$

Within any subset, the image reconstruction is expressed as

$$u_n^{l,k} = u_n^{l,k-1} + \lambda \sum_{m \in B_s} \frac{a_{m,n}}{\sum_{m' \in B_s} a_{m',n}} \frac{b_m - A_m u^{l,k-1}}{a_{m+}}, \quad s = k \bmod T, \tag{5}$$

where l is the index of the outside loop, k is the index of the inside loop, a_{+n} and a_{m+} are the sum of the n^{th} column and m^{th} row of system matrix A, respectively. At the beginning of the first iteration, the initial guess of the image is set to be zero. Then, the reconstructed result at the end of the previous iteration is stored as the initial guess in the current iteration, which is expressed as

$$u^{l-1,K} = u^{l,1}, \tag{6}$$

where K is set to be the iteration number of the inside loop.

In addition, the total variation (TV) is used as a constraint, and a fast gradient-based algorithm is used to minimize the TV [26]. Three merits make it more practicable and competitive. First, the only required parameter to adjust is mainly determined by the object TV value, and the minimized result is not sensitive to the parameter value within a certain range. Second, it always offers a clear image profile with no overshoot or over-smooth phenomenon on the material boundary. Third, the fast convergence rate ensures that the filtered images are almost piecewise constant.

The OS-SART and gradient-based TV minimization algorithms form a complete image update procedure, which can be formulized as

$$u = \arg\min_u \ \|b - Au\|^2 + TV(u). \tag{7}$$

The first part on the right side is called the fidelity term, which is enforced by the OS-SART algorithm. The part next to the fidelity term is called the regularization term, which can be minimized by the gradient-based algorithm. Within one inside loop, one can obtain an optimized result by alternatively applying the aforementioned algorithms to minimize the cost function in Eq. (7). To speed up the convergence, the weighting strategy in the fast iterative shrinkage-thresholding algorithm (FISTA) [27] is introduced, which uses the last two outputs as a feedback to refine the current output.

B. PARAMETER UPDATE

In this part, we use the LLE algorithm to estimate the motion parameters [28]. LLE is a dimensionality reduction algorithm. Similar to the methods of principal component analysis (PCA) [29] and multidimensional scaling (MDS) [30], it is implemented via mapping vectors in a high-dimensional space onto vectors in a low-dimensional space. However, unlike PCA and MDS, which are only appropriate to model linear variabilities in high-dimensional data, the LLE algorithm is very popular for preserving the nonlinear relation among the data points.

Suppose that there is a set of high-dimensional vectors b_v in W_D-dimensional space. They are sufficiently sampled from a smooth underlying data structure. We expect that each data point and its neighbors maintain a sort of linear relationship within a local region so that each data point can be expressed by its neighbors with linear coefficients. Then, the dimensionality reduction procedure is summarized as follows. First, J nearest neighbors for each observation are selected by the metric of Euclidean distance. Second, with these selected neighbors, the corresponding observation

can be reconstructed by computing the linear coefficients. Third, with these computed linear relationships, each high-dimensional observation b_v is mapped to a low-dimensional vector y_v which represent the global internal coordinates.

To compensate for motion artifacts, we use the measured projections to estimate the motion parameters of the imaging object. Because all projections are collected on different time points, they correspond to different object poses. Thus, in this work, the high-dimensional vector b_v represents the v^{th} view of projections, and the mapped low-dimensional vector y_v represents the corresponding motion parameters at the v^{th} time point. We estimate the motion parameters view by view and type by type. For any view, one can densely sample the motion parameters around the current estimation. Then, a set of re-projections $\tilde{b}_{vj}$ are generated with these densely sampled parameters, from which J nearest neighbors can be selected according to the Euclidean distance. If these samples are not far from the ground truth, the original projection can be linearly approximated by its J neighbors,

$$b_v = \sum_{j=1}^{J} w_{vj}\tilde{b}_{vj}, \tag{8}$$

where w_{vj} is the corresponding linear coefficient, which is the contribution of the j^{th} neighbor to the v^{th} observation. To calculate these linear coefficients, a cost function subject to two constraints is introduced,

$$\varepsilon(w, v) = \left\| b_v - \sum_j w_{vj}\tilde{b}_{vj} \right\|^2 \quad s.t. \sum_j w_{vj} = 1, w_{vj} = 0 \quad if\ \tilde{b}_{vj} \notin neighborhood. \tag{9}$$

Minimizing the reconstruction error with these constrained weights can make the reconstructed results invariant to rotations, rescales and translations among the observations and their neighbors. This invariance property makes the reconstructions very stable.

The method to solve Eq. (9) is simple. We begin by calculating the local covariance matrix; each element can be calculated as

$$c_{jk} = (b_v - \tilde{b}_{vj})^T (b_v - \tilde{b}_{vk}). \tag{10}$$

If the neighbor amount is larger than the dimension of an observation, the covariance matrix is singular. For this case, the covariance matrix can be conditioned by adding a small constant onto the diagonal elements. Because solving the constrained Eq. (9) is equivalent to solving the linear equation

$$\sum_j c_{jk} w_{vj} = 1 \quad s.t. \sum_j w_{vj} = 1, \tag{11}$$

one can make a left division of an entire vector by the covariance matrix and enforce the computed weights to sum to one. Now, we have constructed a neighborhood-preserving mapping with these linear coefficients, with which the estimated motion parameters correspond to the v^{th} projection view can be reconstructed

$$y_v = \sum_j w_{vj}\tilde{y}_{vj}, \tag{12}$$

where $\tilde{y}_{vj}$ is the corresponding densely sampled motion parameter for the j^{th} re-projections $\tilde{b}_{vj}$, and y_v is the estimated translation or rotation. The entire described procedure can be used to minimize the first part of Eq. (3), where $\tilde{b}$ is reconstructed with its neighbors.

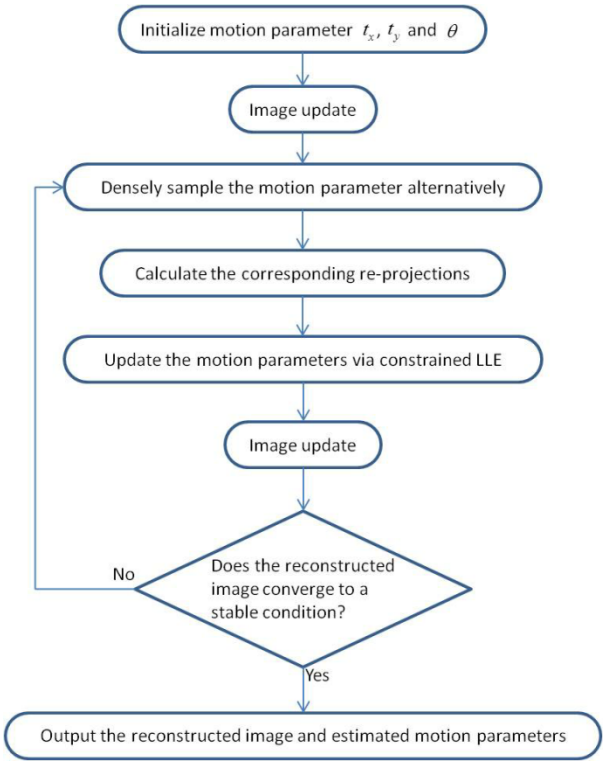

FIGURE 2. Flowchart for implementation of the proposed algorithm.

Because the projections to estimate the motion parameters are truncated, the problem to minimize the cost function in Eq. (3) may contain multiple local minimizers, and the convergence speed can also be degraded. To solve this problem, we consider adding an additional constraint to the cost function Eq. (3). Because of the fast data acquisition of the X-ray CT scanner, the motion speed of the imaging object is naturally much slower than that of the X-ray source. Therefore, the trajectory of the moving object is smooth with lower frequencies, and we assume that the motion parameters can be well fitted to a polynomial function

$$\Phi(v) = \sum_{e=1}^{E} a_e v^e, \tag{13}$$

where a_e is the coefficient of polynomial, and E is the polynomial order. One can use the least-square method to estimate the polynomial coefficients per r iterations. Then, this polynomial function can be used to guide the motion

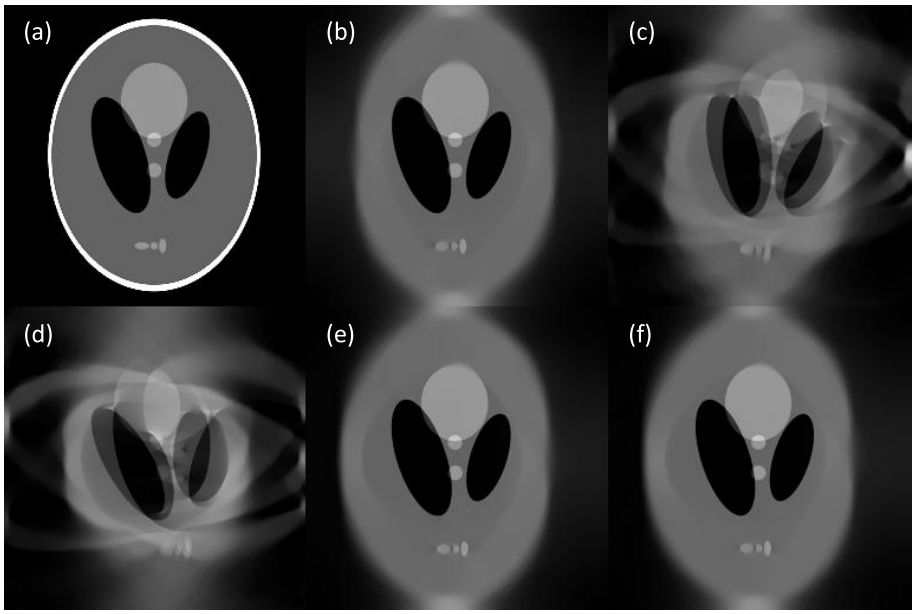

FIGURE 3. Reconstructed phantom images from noise-free projections. (a) is reconstructed from global and motionless projections; (b) is reconstructed from motionless and truncated projections with our motion correction algorithm; (c) and (d) are interior reconstructions from the projections with uniform and spiral motions before correction; (e) and (f) are the counterparts of (c) and (d) with motion correction. The display window is [0 0.5] cm^{-1}.

parameter estimation in future iterations. Because we alternatively update the motion parameters, Eq. (3) can be revised in an iterative form as follows

$$\begin{aligned} t_x^{l+1} &= \arg\min_{t_x} \left\| b - \tilde{b}(t_x) \right\|_2^2 + \delta^l \left\| t_x - \Phi \right\|_2^2 \\ &\quad s.t.\ A(t_x^{l+1}, t_y^l, \theta^l) u_{t_x}^{l+1} = b \\ t_y^{l+1} &= \arg\min_{t_y} \left\| b - \tilde{b}(t_y) \right\|_2^2 + \delta^l \left\| t_y - \Phi \right\|_2^2 \\ &\quad s.t.\ A(t_x^{l+1}, t_y^{l+1}, \theta^l) u_{t_y}^{l+1} = b \\ \theta^{l+1} &= \arg\min_{\theta} \left\| b - \tilde{b}(\theta) \right\|_2^2 + \delta^l \left\| \theta - \Phi \right\|_2^2 \\ &\quad s.t.\ A(t_x^{l+1}, t_y^{l+1}, \theta^{l+1}) u_\theta^{l+1} = b, \end{aligned} \tag{14}$$

where $\delta^l = 1$ when $\mathrm{mod}(l, r) = 0$; otherwise, $\delta^l = 0$. Each view of re-projections $\tilde{b}_v$ can be expressed by Eq. (8), and all views of re-projections make up the re-projection vector $\tilde{b}$. Although Eq. (14) gives a form of minimizing the difference among the entire projection and re-projection vectors, we tackle the projections view by view, and this strategy is equivalent to solving Eq. (14).

For the first iteration, we initialize all motion parameters as zero. Then, the estimated parameters are stored as the initial guesses for the next iteration. In each iteration procedure, we update the motion parameters in order, which are the translation along x direction, translation along y direction and rotation. Each parameter update must follow the image update with the newly estimated motion. With Eq. (14), one can only use the raw projection data to estimate the motion parameters of the object via the regularized mapping. Finally, our motion correction based on the constrained LLE algorithm (MCCL) is summarized as a flowchart in Figure 2.

III. NUMERICAL SIMULATIONS

A. EXPERIMENTAL SETUP

The proposed algorithm is implemented according to the flowchart in Figure 2. To demonstrate its feasibility, we analytically generate three sets of truncated projections of a modified Shepp-Logan phantom with different motions: motionless, uniform motion and a motion with spiral trajectory. For the three groups of datasets, we further introduce noise to test the correction ability of MCCL. As shown in figure 3 (a), the phantom is made of 10 ellipses of different sizes. Its height and width are 9.0 cm and 7.0 cm, respectively. The attenuation coefficient of the outer ring is 1.0 to simulate a skull. The inner part of the phantom with lower attenuation coefficients represents the soft tissues. Both distances from the X-ray source to the origin and from the detector to the origin are 15.0 cm. In total, 512 detector cells are uniformly distributed along a 10.0 cm detector (each detector cell is 0.195 cm long); 360 projections are uniformly collected within 360 degrees, which indicates that the positions of the source and detector are known. The time sampling interval between two adjacent views is set as 0.01 s, i.e., the object motion is sampled 100 times per second.

To quantitatively evaluate the performance of our proposed algorithm, we use several assessment metrics. The root-mean-square error (RMSE) and structural similarity (SSIM) are used to evaluate the reconstructed image quality [31]. Both methods are implemented by comparing the

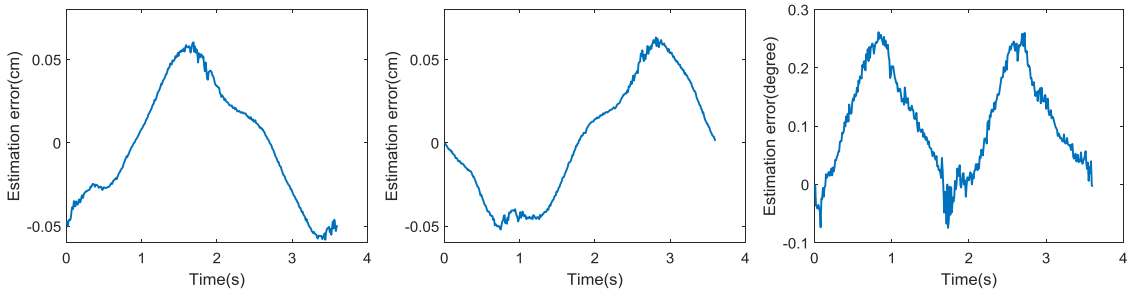

FIGURE 4. Motion correction errors of motionless projections. From left to right, three plots represent the errors for translations along x and y direction and rotation, respectively.

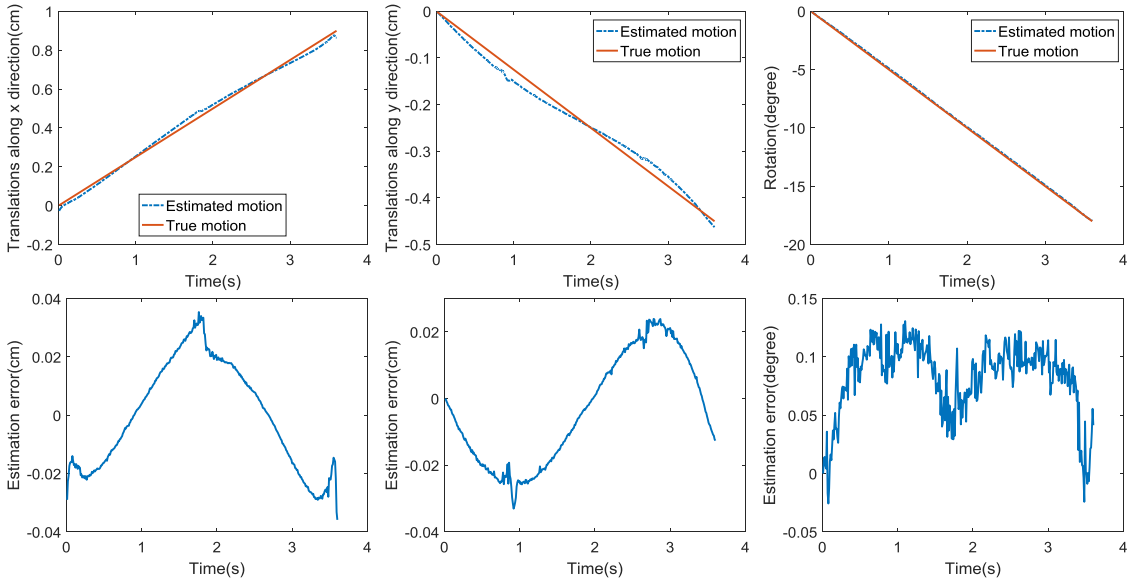

FIGURE 5. Estimated motion parameters and errors of uniform motion. The top row shows the true and estimated motion parameters, and the bottom row gives the corresponding estimation errors. From left to right, three columns are corresponding to the translations along x and y directions and the rotation, respectively.

reconstructed image and ground truth in the field of view. The RMSE measures the pixel intensity error, whereas the SSIM reflects the structural similarity between the reconstructed image and ground truth. In this work, the ground truth is reconstructed from global projections without motion. To quantitatively analyze the motion, a mean translation excursion (MTE) and mean rotation excursion (MRE) are defined as

$$MTE = \int_0^{\tau_V} \|t_\tau\| \, d\tau/\tau_V, \tag{15}$$

and

$$MRE = \int_0^{\tau_V} |\theta_\tau| \, d\tau/\tau_V. \tag{16}$$

After the motion correction, the estimated motion parameters can be used to calculate the corrected MTE and MRE

$$CMTE = \int_0^{\tau_V} \left\|\hat{t}_\tau - t_\tau\right\| d\tau/\tau_V, \tag{17}$$

$$CMRE = \int_0^{\tau_V} \left|\hat{\theta}_\tau - \theta_\tau\right| d\tau/\tau_V, \tag{18}$$

where $\hat{t}_\tau$ and $\hat{\theta}_\tau$ are the estimated translation and rotation at time τ. With these definitions, we evaluate the rectified extent of the motion artifact by computing the relative MTE and MRE as

$$RMTE = CMTE/MTE, \tag{19}$$

$$RMRE = CMRE/MRE. \tag{20}$$

B. NOISE-FREE PROJECTIONS

The reconstructed images contain 256×256 pixels to cover a $10 \times 10cm^2$ region, which is sufficient to display the entire phantom. Parameter r is set to be 30; the iteration number of image update K is set to be 10; the order of the polynomial E is set to be 4 and 18 for the uniform motion and spiral motion, respectively. Figure 3 shows the reference image and reconstructed images from projections with different motions before and after the motion corrections. The corrected image from motionless projections has a similar central structure in the field of view, which demonstrates that the proposed algorithm is convergent. The corresponding motion estimation errors are shown in figure 4. The

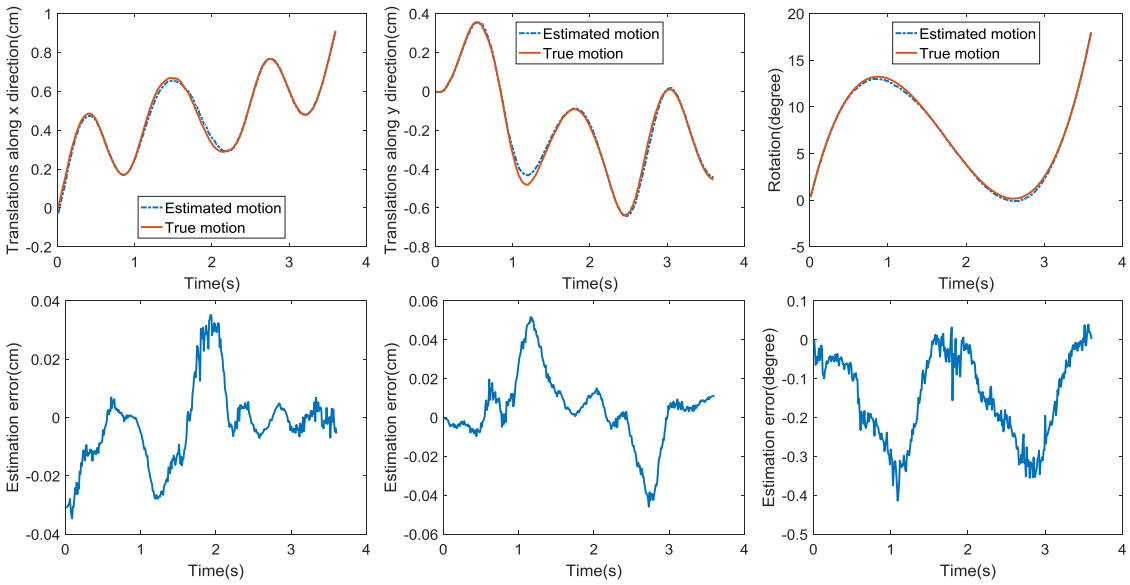

FIGURE 6. The same as figure 5 but for spiral motion.

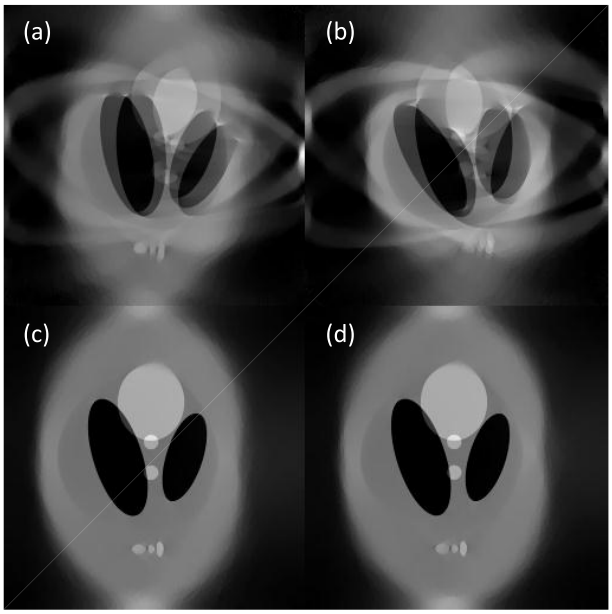

FIGURE 7. Reconstructed images before and after motion corrections from noisy projections. The top row shows the images without motion corrections and the bottom row shows the images with motion corrections. The left column corresponds to the uniform motion and the right column corresponds to the spiral motion. The display window is [0 0.5]cm^{-1}.

estimated offsets along the x and y directions have maximal absolute deviations of approximately 0.05 cm, which is approximated to an image pixel size possibly because the estimation error is related to the mismatch between discrete and analytical image models. The image quality is poor for the reconstructed images without compensation from motion estimation. Uniform motion makes the image look like a superposition with two phantoms, and the motion with a spiral trajectory thoroughly blurs the object structures. Both images fail to offer correct information of the object.

TABLE 1. Quantitative evaluation results of the proposed algorithm for motion corrections.

	Uniform Motion		Spiral Motion	
	Noise-free	Noisy	Noise-free	Noisy
RMSE	0.0047	0.0085	0.0055	0.0071
SSIM	0.9439	0.8931	0.9423	0.8993
CMTE(cm)	0.0280	0.0962	0.0185	0.0756
RMTE	5.55%	19.06%	3.27%	13.39%
CMRE(degree)	0.0168	0.1692	0.1491	0.2126
RMRE	0.19%	1.87%	2.12%	3.03%

In contrast, the reconstructed images are very similar to the reference after motion corrections, and part of the neighbor region is comparable to the reference. Figures 5 and 6 are the motion parameters and estimation errors for the uniform and spiral motions, respectively. The estimated rotation parameters appear more accurate compared to their magnitudes. These results are consistent with the estimation for the motionless object: the maximal absolute error is similar to the image pixel size. Furthermore, the corrected offset errors along x and y directions are always enlarged when the projection direction is approximately parallel to the estimation offset directions. This type of error may be caused by the truncated projections and weakness of distance perception. In summary, the corrected motion parameters are very similar to the ground truth.

C. NOISY PROJECTIONS

Poisson noise is superimposed to the raw projections by assuming 10^5 incident photons for each detector cell. Parameters r, K and E are identical to those in the noise-free cases.

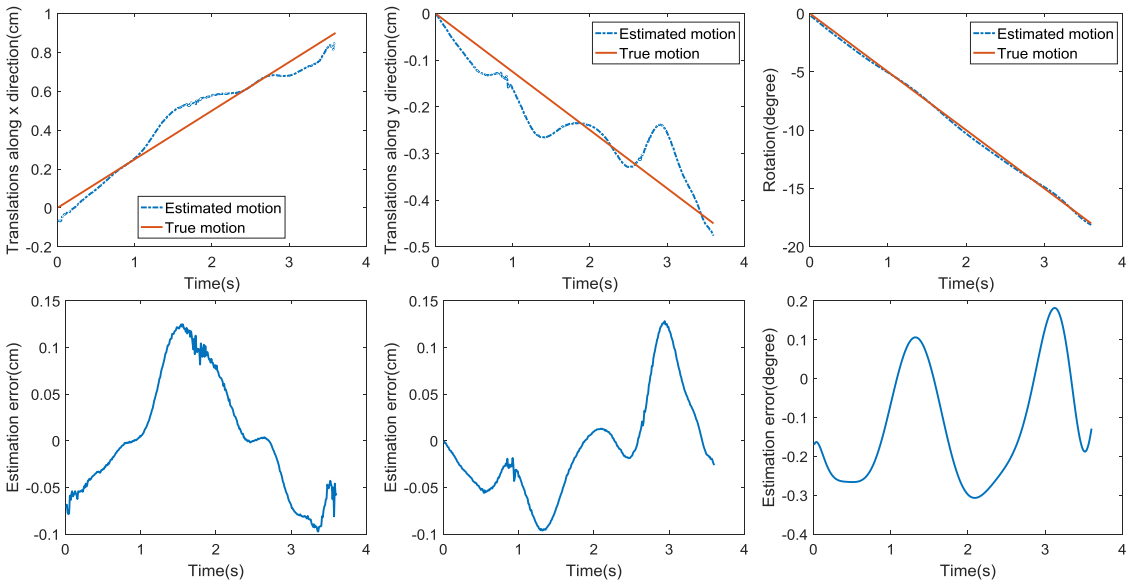

FIGURE 8. The same as figure 5 but from noisy projections assuming 10^5 incident photons per detector cell.

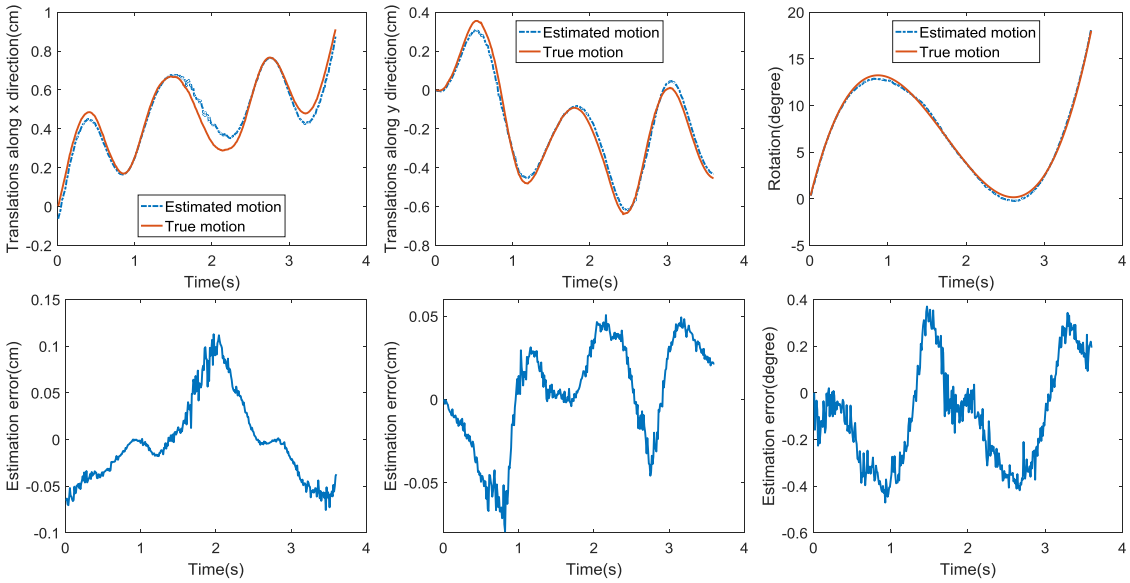

FIGURE 9. The same as figure 6 but from noisy projections assuming 10^5 incident photons per detector cell.

Figure 7 displays the reconstructed images with and without motion corrections. The corrected images have very similar qualities to the noise-free ones. The two central small ellipses are plump, and the boundaries of two narrow and dark ellipses are easily distinguished. Although the structure composed of three smaller ellipses outside the FOV is slightly distorted, it does not affect the required information. The estimated motion parameters and their corresponding errors are shown in figures 8 and 9. Their accuracies are slightly degraded because of Poisson noise. The error magnitudes are approximately 2- to 3-fold that of the corresponding noise-free cases. Fortunately, the estimated motion parameters always fluctuate near the ground truth, which can ensure better reconstructed image qualities. The estimation errors obey the observed rules of the noise-free cases, and the estimated rotation parameters show a higher accuracy than translations.

D. QUANTITATIVE EVALUATION RESULTS

The quantitative evaluation results for the proposed algorithm are summarized in Table 1. The RMSE results reveal that the corrected images remain the original attenuation for different materials because they are relatively small. The similarity of

corrected reconstructions and reference is considered high in terms of visual observation and SSIM indices. Both RMSE and SSIM results are affected by noise with slightly enlarged amplitudes of variation. All CMTE indices for noisy and noise-free cases are in the same magnitude of pixel size, and those deviations are acceptable. The RMTE indices show that the correction for translation is more sensitive to noise. Both CMRE and RMRE indices show good corrections for rotation in both noise-free and noisy cases because the image reconstruction is more sensitive to the rotation errors. In other words, for the same motion artifact level, the rotation error is smaller than the translational motion error.

IV. DISCUSSIONS AND CONCLUSIONS

In section III, several groups of datasets are applied to demonstrate the feasibility and evaluate the performance of the proposed MCCL algorithm. The motion estimation results show that the MCCL has a strong capability to estimate the motion parameters from truncated projections. As far as the authors know, this algorithm is the first of its kind for motion parameter estimation only from truncated projections in the CT field. To generate projections of a moving object, the translations and rotation are set to be large compared to the phantom size. The large magnitude of motion induces severe artifacts in the initial reconstruction without motion compensation. Considering the truncation of projections, the FOV, which can be illustrated by all projections, is small. It is difficult to map the truncated projection space with very limited available information onto the motion parameter space. Synthesizing all difficult conditions, the reconstructed images and accuracy of the estimated motion parameters are decent.

In the numerical implementation of the proposed algorithm, many details must be discussed. Regarding the selection of the polynomial order E, we hope that the MCCL is appropriate for most cases, and a relatively large E is desirable. Nevertheless, the computer precision enforces an upper limit. Meanwhile, a moderate value can theoretically suppress the artifact caused by the noise and mismatch. Finally, E is limited in the range of 4-18 depending on the motion complexity.

Translations and rotations reveal different sensitivities during the motion corrections. The results of quantitative evaluations show that the correction for rotation is always more accurate than those of translations. In addition, the correctable range for rotation is wide (more than 90 degrees), whereas the correctable range for translation is limited. This difference is consistent with the common sense that image reconstruction is more sensitive to the errors of rotation angles. When the object continuously moves out of the FOV, the corresponding motion parameters cannot be successfully estimated. Similar to the interior reconstruction, relative to the object size, the smaller the FOV is, the worse the estimation accuracy is for a given motion pattern. Therefore, to guarantee satisfied estimation accuracy, the FOV could not be too small. Beside, we must ensure a fixed region of the object always stay in the FOV, that is, the minimum size of FOV also depends on the motion range for a satisfied motion estimation. For practical applications, we recommend that the FOV radius should be at least 1/3 of the object radius.

The parameter sampling intervals can also determine the motion estimation results. In our experiments, the sampling interval for translation is smaller than the correction error. If the interval is large, the corrected parameters will fluctuate around the ground truth. The sampling interval for rotation is not as sensitive. However, the sampling range must be wide at the beginning; otherwise, the motion correction will not converge. Thus, we apply a multi-scale scheme to solve the problems of convergence and accuracy: the sampling interval can be decreased from a large value to a small value during the iterations. In our numerical simulations, the sampling interval for translations is set to be 0.0001cm. For rotation, we set the sampling interval as 2 degree in the first 100 iterations and 0.002 degree for the rest iterations. For any motion parameter, we symmetrically extract 21 uniform sampling points around current estimation.

The parameter r is the period that we valid the constraint term. Although the constraint method can improve the accuracy of motion estimation, enforcing the motion trajectory into a polynomial form for each iteration may affect the convergence rate. We try to weaken this kind of conflict by setting a period to employ the constraint term.

TV as a regularization term for image update is another factor that affects the correction accuracy. On one hand, a moderate TV intensity can effectively suppress the noise and help to solve the interior problem. On the other hand, a strong TV regularization makes the reconstructed image over-smooth and decreases the accuracy of the estimated motion parameters.

The most difficult challenge is how to use the truncated projections to estimate the motion parameters. Theoretically, each projection view must correspond to a group of motion parameters. The mapping relationship is fixed, although the projection is truncated. However, the accuracy will be affected by the data truncation. To promote the stability of this mapping, we can improve the image and projection resolutions. However, the resolution improvement for projections will lead to more severe noise or an increase in radiation dose, and a greater total pixel number will increase the computation complexity. To overcome these problems, we add a regularization term onto the LLE-based mapping to reduce the deviations of the estimated motion parameters. The numerical simulation results confirm the merits of this strategy.

The motion correction results for noisy projections show that MCCL can be slightly affected by noise. In the near future, we will investigate other possible regularization terms to help suppress the noise. The accuracy of the reconstructed image is an important element to determine the estimated motion parameters. We hypothesize that some valid prior information may help to improve the noise suppression performance.

In conclusion, we have proposed a constrained LLE-based algorithm to compensate for motion artifacts from truncated projections. This algorithm is the first of its kind for motion parameter estimation only from truncated projections in the CT field. The algorithm is implemented by alternatively updating the reconstructed image and motion parameters. Numerical simulations with and without noise demonstrate the feasibility of MCCL, which verifies that the truncated projections DO encode motion information of an object. We believe that the proposed MCCL possesses the developmental prospect and potential application value in the near future.

ACKNOWLEDGMENT

The authors are grateful to M. Chen in Chongqing University for his help on our algorithm implementation.

REFERENCES

[1] F. Noo, R. Clackdoyle, and J. D. Pack, "A two-step Hilbert transform method for 2D image reconstruction," *Phys. Med. Biol.*, vol. 49, no. 17, p. 3903, 2004.
[2] M. Defrise, F. Noo, R. Clackdoyle, and H. Kudo, "Truncated Hilbert transform and image reconstruction from limited tomographic data," *Inverse Problems*, vol. 22, no. 3, p. 1037, 2006.
[3] J. Yang, H. Yu, M. Jiang, and G. Wang, "High-order total variation minimization for interior tomography," *Inverse Problems*, vol. 26, no. 3, p. 035013, 2010.
[4] W. Han, H. Yu, and G. Wang, "A general total variation minimization theorem for compressed sensing based interior tomography," *J. Biomed. Imag.*, vol. 2009, Jan. 2009, Art. no. 125871.
[5] H. Yu, J. Yang, M. Jiang, and G. Wang, "Supplemental analysis on compressed sensing based interior tomography," *Phys. Med. Biol.*, vol. 54, no. 18, p. N425, 2009.
[6] H. Yu and G. Wang, "Compressed sensing based interior tomography," *Phys. Med. Biol.*, vol. 54, no. 9, p. 2791, 2009.
[7] G. Wang and H. Yu, "Exact local computed tomography based on compressive sampling," U.S. Patent 13 264 843, Apr. 10, 2014.
[8] Y. Liu, H. Liu, Y. Wang, and G. Wang, "Half-scan cone-beam CT fluoroscopy with multiple X-ray sources," *Med. Phys.*, vol. 28, no. 7, pp. 1466–1471, 2001.
[9] H. Yu and G. Wang, "Feldkamp-type VOI reconstruction from super-short-scan cone-beam data," *Med. Phys.*, vol. 31, pp. 1357–1362, Jun. 2004.
[10] J. Hsieh, *Computed Tomography: Principles, Design, Artifacts, and Recent Advances*, vol. 114. Bellingham, WA, USA: SPIE, 2003.
[11] C. R. Crawford and K. F. King, "Computed tomography scanning with simultaneous patient translation," *Med. Phys.*, vol. 17, no. 6, pp. 967–982, Nov. 1990.
[12] F. Noo, R. Clackdoyle, C. Mennessier, T. A. White, and T. J. Roney, "Analytic method based on identification of ellipse parameters for scanner calibration in cone-beam tomography," *Phys. Med. Biol.*, vol. 45, no. 11, p. 3489, 2000.
[13] H. Yu, Y. Wei, J. Hsieh, and G. Wang, "Data consistency based translational motion artifact reduction in fan-beam CT," *IEEE Trans. Med. Imag.*, vol. 25, no. 6, pp. 792–803, Jun. 2006.
[14] H. Yu and G. Wang, "Data consistency based rigid motion artifact reduction in fan-beam CT," *IEEE Trans. Med. Imag.*, vol. 26, no. 2, pp. 249–260, Feb. 2007.
[15] W. Wein, A. Ladikos, and A. Baumgartner, "Self-calibration of geometric and radiometric parameters for cone-beam computed tomography," in *Proc. 11th Int. Met. Fully Three-Dimensional Image Reconstruct. Radiol. Nucl. Med.*, Jul. 2011, pp. 1–4.
[16] G. H. Chen and S. Leng, "A new data consistency condition for fan-beam projection data," *Med. Phys.*, vol. 32, no. 4, pp. 961–967, Apr. 2005.
[17] M. S. Levine, E. Y. Sidky, and X. Pan, "Consistency conditions for cone-beam CT data acquired with a straight-line source trajectory," *Tsinghua Sci. Technol.*, vol. 15, no. 1, pp. 56–61, Feb. 2010.
[18] M. Defrise, F. Noo, and H. Kudo, "Improved two-dimensional rebinning of helical cone-beam computerized tomography data using John's equation," *Inverse Problems*, vol. 19, no. 6, p. S41, 2003.
[19] D. Panetta, N. Belcari, A. Del Guerra, and S. Moehrs, "An optimization-based method for geometrical calibration in cone-beam CT without dedicated phantoms," *Phys. Med. Biol.*, vol. 53, no. 14, p. 3841, 2008.
[20] V. Patel, R. N. Chityala, K. R. Hoffmann, C. N. Ionita, D. R. Bednarek, and S. Rudin, "Self-calibration of a cone-beam micro-CT system," *Med. Phys.*, vol. 36, no. 1, pp. 48–58, Jan. 2009.
[21] M. Chen, Y. Xi, W. Cong, B. Liu, B. Wei, and G. Wang, "X-ray CT geometrical calibration via locally linear embedding," *J. X-Ray Sci. Technol.*, vol. 24, no. 2, pp. 241–256, 2016.
[22] T. Sun, J.-H. Kim, R. Fulton, and J. Nuyts, "An iterative projection-based motion estimation and compensation scheme for head X-ray CT," *Med. Phys.*, vol. 43, no. 10, pp. 5705–5716, Oct. 2016.
[23] R. Clackdoyle and L. Desbat, "Data consistency conditions for 2D truncated parallel projections," in *Proc. 3rd Int. Conf. Image Formation X-Ray Comput. Tomogr.*, Salt Lake City, UT, USA, 2014, pp. 319–323.
[24] H. Yu, G. Wang, J. Yang, J. D. Pack, M. Jiang, and B. De Man, "Data consistency condition for truncated projections in fan-beam geometry," *J. X-Ray Sci. Technol.*, vol. 23, no. 5, pp. 627–638, 2015.
[25] G. Wang and M. Jiang, "Ordered-subset simultaneous algebraic reconstruction techniques (OS-SART)," *J. X-Ray Sci. Technol.*, vol. 12, no. 3, pp. 169–177, Jan. 2004.
[26] A. Beck and M. Teboulle, "Fast gradient-based algorithms for constrained total variation image denoising and deblurring problems," *IEEE Trans. Image Process.*, vol. 18, no. 11, pp. 2419–2434, Nov. 2009.
[27] A. Beck and M. Teboulle, "A fast iterative shrinkage-thresholding algorithm for linear inverse problems," *SIAM J. Imag. Sci.*, vol. 2, no. 1, pp. 183–202, 2009.
[28] S. T. Roweis and L. K. Saul, "Nonlinear dimensionality reduction by locally linear embedding," *Science*, vol. 290, no. 5500, pp. 2323–2326, Dec. 2000.
[29] I. Jolliffe, *Principal Component Analysis*. Hoboken, NJ, USA: Wiley, 2002.
[30] T. F. Cox and M. A. Cox, *Multidimensional Scaling*. Boca Raton, FL, USA: CRC Press, 2000.
[31] Z. Wang, A. C. Bovik, H. R. Sheikh, and E. P. Simoncelli, "Image quality assessment: From error visibility to structural similarity," *IEEE Trans. Image Process.*, vol. 13, no. 4, pp. 600–612, Apr. 2004.

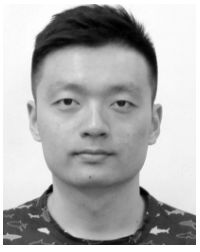

MIAOSHI WANG received the B.Sc. degree in electronic information science and technology from the College of Electronic Science and Engineering, Jilin University, in 2011, where he is currently pursuing the Ph.D. degree in circuit and system. His research interests mainly focus on computed tomography.

SHUXU GUO received the B.Sc., M.Sc., and Ph.D. degrees in electronic engineering from Jilin University, Changchun, China, in 1982, 1989, and 2006, respectively. Since 2000, he has been a Professor with the State Key Laboratory on Integrated Optoelectronics, College of Electronic Science and Engineering, Jilin University, where he was involved in the reliability of semiconductor devices and the digital image processing and analysis.

HENGYONG YU (SM'06) received the bachelor's degrees in information science and technology and computational mathematics and the Ph.D. degree in information and communication engineering from Xi'an Jiaotong University in 1998 and 2003, respectively. He was an Assistant Professor and Associate Professor with the College of Communication Engineering, Hangzhou Dianzi University, from 2003 to 2004. From 2004 to 2006, he was a Post-Doctoral Fellow and an Associate Research Scientist with the Department of Radiology, University of Iowa, Iowa City, IA, USA. From 2006 to 2010, he was a Research Scientist and the Associate Director of CT Lab, Biomedical Imaging Division, VT-WFU School of Biomedical Engineering & Sciences, Virginia Tech, Blacksburg, VA, USA. From 2010 to 2014, he was an Assistant Professor with the Biomedical Engineering Department, Wake Forest University Health Sciences. He is currently an Associate Professor and the Director of the Imaging and Informatics Lab, Department of Electrical and Computer Engineering, University of Massachusetts at Lowell, Lowell, MA, USA. He has authored or coauthored over 120 peer-reviewed journal papers with an H-index of 31 according to Google Scholar. His interests include computed tomography and medical image processing. He is a Senior Member of the IEEE Engineering in Medicine and Biology Society, and a member of the American Association of Physicists in Medicine and the Biomedical Engineering Society. In 2005, he was honored for an outstanding doctoral dissertation by Xi'an Jiaotong University. He received the first prize for a best natural science paper from the Association of Science & Technology of Zhejiang Province. In 2012, he received an NSF CAREER Award for the development of CS-based interior tomography. He is the founding Editor-in-Chief of the *JSM Biomedical Imaging Data Papers*. He serves as an Editorial Board Member of *Signal Processing*, IEEE Access, the *Journal of Medical Engineering*, and *CT Theory and Applications*.